3D concrete printing using computational fluid dynamics: Modeling of material extrusion with slip boundaries

El Abbaoui, Khalid; Al Korachi, Issam; El Jai, Mostapha; Šeta, Berin; Mollah, Md Tusher

Published in:
Journal of Manufacturing Processes

Link to article, DOI:
10.1016/j.jmapro.2024.03.042

Publication date:
2024

Document Version
Publisher's PDF, also known as Version of record

Journal of Manufacturing Processes 118 (2024) 448–459

Contents lists available at ScienceDirect

Journal of Manufacturing Processes

journal homepage: www.elsevier.com/locate/manpro

3D concrete printing using computational fluid dynamics: Modeling of material extrusion with slip boundaries

Khalid El Abbaoui [a,**], Issam Al Korachi [a], Mostapha El Jai [a,b], Berin Šeta [c], Md. Tusher Mollah [c,*]

[a] Euromed Center of Research, Euromed Polytechnic School, Euromed University of Fes, Fes, Morocco
[b] Mechanic, Mechatronic and Command Laboratory, ENSAM-Meknes, Moulay Ismail, University, Meknes, Morocco
[c] Department of Civil and Mechanical Engineering, Technical University of Denmark, 2800 Kgs. Lyngby, Denmark

ARTICLE INFO

Keywords:
3D concrete printing
Computational fluid dynamics
Cross-sectional shapes
Slip boundary conditions
Generalized Newtonian fluid model
Elasto-viscoplastic fluid model

ABSTRACT

This paper investigates the role of slip boundary conditions in computational fluid dynamics modeling of material extrusion and layer deposition during 3D concrete printing. The mortar flow governed by the Navier-Stokes equations was simulated for two different slip boundary conditions at the extrusion nozzle wall: no-slip and free-slip. The simulations were conducted with two constitutive models: a generalized Newtonian fluid model and an elasto-viscoplastic fluid model. The cross-sectional shapes of up to three printed layers were compared to the experimental results from literature for different geometrical- and speed-ratios. The results reveal that employing free-slip boundary conditions at the extrusion nozzle wall improves layer-mimicking quality for both constitutive models, indicating the presence and importance of a lubricating layer of fine particles at the concrete-solid wall interface. This enhanced performance is primarily due to the observed decrease in extrusion pressure that minimizes layer height- and width-deviations compared to the experimental prints. Furthermore, the free-slip boundary conditions play an important role in predicting the multilayer prints, its deformation and groove shapes.

1. Introduction

3D Concrete Printing (3DCP) is on the way to becoming the leading technique adopted in the building sector. Unlike traditional methods, 3DCP enables the additive manufacture of complex geometries and free-form structures with minimal labor and reduced construction costs [1]. This innovative technique involves mixing, pumping, and then extruding concrete through a nozzle mounted on a robotic arm or traveling crane [2–4]. The concrete is deposited layer by layer along planned path to build structural elements without the need for formwork [5–7]. In the last decade, the 3DCP has gained the interest of researchers and engineers worldwide. Their focus lies in understanding the process of concrete shaping [8–10], identifying a range of acceptable rheological properties for printable cementitious materials [11–13], and developing 3D printing strategies for large-scale structures [14–16].

Flowability of concrete plays a crucial role in technical and economic feasibility during 3DCP. However, to ensure successful layer deposition, the concrete flow must be consistent to avoid voids, gaps, or weak spots within the printed layers, making it uniform and thus reducing the deviations from the intended geometry [17,18]. This requires that the pumped material contains sufficient water to facilitate the formation of a lubricating layer of fine particles at the interface between the solid wall and the concrete [19–21]. This layer occurs due to dynamic segregation, where the coarse particles of the mixture migrate towards the low-shear zones, typically the center of the nozzle [22,23]. The lubricating layer possesses significantly lower rheological properties than pumped concrete, enabling the concrete block to slip consistently through the pipe and the nozzle. Generally, the slip velocity is assumed to depend on the shear stress at the boundary between the concrete and the nozzle wall [24,25], while several experiments suggest that slip velocity also depends on normal stress at the wall [26–28]. Nonetheless, there is a lack of understanding of how the slip phenomenon affects deposited layers in 3DCP processes [29]. This ultimately underscores the need for a more thorough investigation.

Computational Fluid Dynamics (CFD) has become an essential tool for understanding and improving 3DCP. With its ability to simulate and analyze the complex aspects of the process, CFD plays a crucial role in optimizing concrete formulation and simulating flow inside pumping

** Corresponding author.
* Correspondence to: M.T. Mollah, Department of Civil and Mechanical Engineering, Technical University of Denmark, Denmark.
E-mail addresses: k.elabbaoui@ueuromed.org (K. El Abbaoui), mtumo@dtu.dk (Md.T. Mollah).

https://doi.org/10.1016/j.jmapro.2024.03.042
Received 3 February 2024; Accepted 12 March 2024
Available online 3 April 2024

pipe [30,31], extrusion through a nozzle [32,33], influence of printing parameters and final shape of prints [34,35], as well as applying different reinforcement methods to the process [36,37], reproducing multi-layer printing [38], etc. Research and development of more accurate CFD models have been driving the core understanding of 3DCP and sustainable construction. Comminal et al. [29] used CFD to analyze the cross-sectional shapes of printed layers. The proposed CFD model was thereafter used to investigate the influence of the printing parameters on the layer shape [39]. The studies by Mollah et al. [40–42] involved simulating and explaining the deformation of subsequent layers as well as examining how to assure stability while minimizing the deformation at the bottom. CFD models can mimic the printing of corners and predict their precision. This, as demonstrated by [43,44], empowers engineers to fine-tune printing parameters for sharp, well-defined corners, crucial for architectural and structural integrity. CFD models like those in [45,46] can predict printing strategies that ensure proper integration and load transfer between concrete and reinforcement, critical for structural stability. Šeta et al. [47–49] delved into the realm of fiber-reinforced composites, using CFD to predict the orientation of fibers within printed strands. This knowledge is invaluable for tailoring printing parameters to achieve desired mechanical properties in the final structure.

As illustrated by the cited studies, CFD simulations help elucidate the complex interactions between material properties, processing parameters, and final printed structures. However, current modeling of cementitious material extrusion and layer deposition typically employs no-slip boundary conditions on all solid objects [50,51]. This assumes zero relative velocity between the extruded material and the nozzle surface upon contact. In fact, there are situations in which slip behavior occurs, notably in the case of the concrete flow in contact with a wall [21]. Ongoing research aims to refine existing models and integrate slip behavior more accurately into simulations for a more predictive and optimized 3DCP paradigm [52]. This is the main objective of the present work in numerically investigating the impact of a free-slip mortar flow inside the nozzle on three deposited layers. This feature could be an essential element in the CFD modeling of 3D concrete printing processes.

This study investigates the influence of different slip boundary conditions on numerical simulations of 3D concrete printing for two rheological models: a generalized Newtonian fluid (GNF) model and an elasto-viscoplastic (EVP) fluid model. The first part presents a detailed description of the methodology of the study starting with the governing equations and rheological modeling, computational domain and boundary conditions, numerical methods and simulations benchmark. At the end of this part, a mesh sensitivity for one-layer cross sections is performed. The second part discusses the influence of the critical shear rate for GNF and the slip boundary conditions for different printing conditions for both GNF and EVP models. Furthermore, the influence of the slip boundary conditions on the extrusion pressure and strain rate is discussed. Note that the numerical results are compared to the experimental results of Comminal et al. [29] in the case of single-layer deposition and to the ones of Spangenberg et al. [38] in the case of multi-layer deposition. The final section summarizes the main conclusions of the study.

2. Methodology

2.1. Governing equations and rheological modeling

The flow of fresh mortar is modeled by the Navier-Stokes equations for incompressible fluids of constant density ρ as follows:

$$\frac{\partial u_i}{\partial x_i} = 0 \tag{1}$$

$$\frac{\partial u_i}{\partial t} + u_j \frac{\partial u_i}{\partial x_j} = -\frac{1}{\rho}\frac{\partial p}{\partial x_i} + g_i + \frac{\partial \sigma_{ij}}{\partial x_j} \tag{2}$$

where u_i is the velocity component in the i-th direction, $x_{i=1,2,3}$ is the i-th coordinate in the Cartesian space, t is the time, p is the local pressure, g_i is the gravitational acceleration, and σ_{ij} is the constitutive shear stress tensor. Eq. (1) describes the continuity equation of incompressible materials, thereby Eq. (2) denotes the momentum conservation equation.

The constitutive shear stress tensor is modeled using two constitutive models, an inelastic Generalized Newtonian Fluid (GNF) model, and an elasto-viscoplastic (EVP) fluid model, which are described as a time-independent as follows.

2.1.1. Generalized Newtonian fluid model

The GNF model is obtained by replacing the constant viscosity of the Newtonian fluid model with a shear rate-dependent apparent viscosity in which the yielding point and shear-thinning of the material are considered. The constitutive shear stress tensor is modeled with the GNF model in the isothermal and isotropic flow regime, as follows:

$$\sigma_{ij} = 2\eta_{app}(\dot{\gamma})D_{ij} \tag{3}$$

where $\eta_{app}(\dot{\gamma})$ is the shear rate-dependent apparent viscosity of the material, and D_{ij} is the linearized strain rate tensor given by:

$$D_{ij} = \frac{1}{2}\left(\frac{\partial u_j}{\partial x_i} + \frac{\partial u_i}{\partial x_j}\right) \tag{4}$$

The shear rate $\dot{\gamma}$ is defined as the magnitude of the linearized strain rate tensor, yielding:

$$\dot{\gamma} = \sqrt{2\sum_{i,j} D_{ij}D_{ij}} \tag{5}$$

The yielding and shear-thinning of fresh mortar are described through their apparent viscosity by using a viscoplastic Bingham constitutive model, the most commonly used to describe the rheological behavior of cementitious materials [53]. The special feature of this model is the yield stress τ_Y, which defines the shear stress threshold for a non-zero strain rate. As a result, the apparent viscosity of the material becomes infinitely large at very low shear rates, indicating a solid-like behavior of mortar and creating a singularity problem issue in the numerical simulations. To avoid this problem, a bi-viscous constitutive equation [54] is employed in which small deformations are allowed by setting a maximum apparent viscosity for the low shear rate region, yielding:

$$\eta_{app}(\dot{\gamma}) = \begin{cases} \eta_{app.max} & for\ \dot{\gamma} < \dot{\gamma}_c \\ \dfrac{\tau_Y}{\dot{\gamma}} + \mu_p & for\ \dot{\gamma} \geq \dot{\gamma}_c \end{cases} \tag{6}$$

where μ_p denotes the plastic viscosity of the fresh mortar, $\dot{\gamma}_c$ is the critical shear rate which separate the two flow regimes, and $\eta_{app.\max} = \tau_Y/\dot{\gamma}_c + \mu_p$ is the maximum apparent viscosity corresponding to the lower shear rate.

2.1.2. Elasto-viscoplastic fluid model

The EVP fluid model describes an elastic behavior for which the applied stresses are below the yield stress, characterized by recoverable strain due to an elastic shear modulus, G. Beyond the yield stress, it transitions to a viscoplastic regime where plastic flow occurs alongside viscous dissipation. This intricate behavior can be represented by a combination of Hookean spring (representing elastic shear stress), dashpot (representing viscous shear stress), and dry sliding element (accounting for plastic strain through yield stress). The constitutive shear stress tensor of the EVP fluid is a summation of elastic and viscous shear stress tensors, as follows:

$$\sigma_{ij} = \sigma_{ij}^E + \sigma_{ij}^V \tag{7}$$

The specific goal of the EVP model is to solve the deviatoric elastic shear stress tensor σ_{ij}^{sE} according to the local strain of the incompressible

material. For small strains, σ_{ij}^{*E} is computed by the isotropic Hooke's law as a linear function of the deviatoric strain tensor ε_{ij} through the elastic shear modulus:

$$\sigma_{ij}^{*E} = 2G\varepsilon_{ij} \tag{8}$$

The overall non-linear elasticity of the mortar is predicted by the incremented strain tensor that is solved by integrating the strain rate tensor, D_{ij}, over a small-time step $\Delta t = t - t_0$:

$$\varepsilon_{ij}(t) = \varepsilon_{ij}(t_0) + \Delta t D_{ij} \tag{9}$$

A differential form of the incremental elastic shear stress tensor is given as a combination of temporal and material derivatives:

$$\frac{\partial \sigma_{ij}^{*E}}{\partial t} + \frac{\partial u_i \sigma_{ij}^{*E}}{\partial x_i} - \left(\sigma_{ij}^{*E} \cdot W_{ij} + W_{ij}^{T} \cdot \sigma_{ij}^{*E}\right) = 2GD_{ij} \tag{10}$$

Eq. (10) expresses the total rate of change in the elastic shear stress tensor, considering temporal variations at a fixed location and spatial changes due to advection and rotation of stress as the material moves, where W_{ij} is the vorticity tensor, given by:

$$W_{ij} = \frac{1}{2}\left(\frac{\partial u_j}{\partial x_i} - \frac{\partial u_i}{\partial x_j}\right) \tag{11}$$

The elastic shear stress tensor of the yielded EVP mortar is approximated as a function of the yield stress τ_Y, expressed as:

$$\sigma_{ij}^{E} = min\left(1, \frac{\tau_Y}{\tau_{vM}}\right)\sigma_{ij}^{*E} \tag{12}$$

where τ_{vM} is the von Mises yield stress criteria applied to assume the material yield point, defined by:

$$\tau_{vM} = \sqrt{\frac{2}{3} II_{\sigma_{ij}^{*E}}} \tag{13}$$

where $II_{\sigma_{ij}^{*E}} = tr\left(\left(\sigma_{ij}^{*E}\right)^2\right)$ is the second invariant of $(\sigma^{*E})^2$. The condition for material yielding stipulates that τ_{vM} exceeds the yield stress limit:

$$\tau_{vM} \geq \tau_Y \tag{14}$$

The viscoplastic regime is represented by the viscous shear stress tensor, defined as:

$$\sigma_{ij}^{V} = 2\mu_p D_{ij} \tag{15}$$

The Table 1 below provides a summary of the material properties employed in the simulations.

Table 1
Rheology and concrete properties [29].

Material properties	Symbols	Corresponding values and units
Density	ρ	2100 kg/m^3
Plastic viscosity	μ_p	7.5 Pa·s
Yield stress	τ_Y	630 Pa
Critical shear rate (GNF model)	$\dot{\gamma}_c$	0.01 s^{-1}
Elastic shear modulus (EVP model)	G	2·10^5 Pa

2.2. Computational domain and boundary conditions

The computational domain is a rectangular box designed to represent the mortar extrusion and layer deposition. The key elements involved in this phase are the extrusion nozzle, the substrate, and the material being extruded (Fig. 1.a). The extrusion nozzle is a hollow cylinder with an inner diameter, D = 25 mm, and a thickness of 2 mm. The extrusion nozzle is stationary at the beginning and starts to move with the printing speed, V [mm/s], as soon as the extruded material touches the substrate. The material is extruded at an extrusion speed, U [mm/s]. The substrate is a non-moving plate that is designed to support the deposited material. The entire computational domain is discretized with a uniform Cartesian mesh. Solid components are represented in the computational domain by a cell porosity technique called Fractional Area/Volume Obstacle Representation (FAVOR) method [55].

The interface between the fresh cementitious mortar and substrate is assigned to a no-slip boundary conditions, whereas at the nozzle, the slip boundary conditions are varied. Two types of slip boundary conditions have been varied numerically: no-slip and free-slip boundary conditions. A constant extrusion speed is assigned at the top of the computational domain and a fluid region is created inside the nozzle to allow the fresh concrete to flow and exit the nozzle orifice with a fully developed profile. The bottom boundary of the domain is set as a stationary wall and contains the substrate. The other domain boundaries are set as continuative, implying zero velocity vector field derivative across these boundaries (Fig. 1.b).

2.3. Numerical methods and simulations benchmark

To accurately model the intricate processes involved in 3D concrete printing and establish a reliable benchmark for future simulations, this paper employed a combination of robust numerical methods and meticulously defined printing parameters. The governing equations of the fresh concrete flow are discretized using the finite volume method and then solved by means of the FLOW-3D® solver (version 12.0, 2019) [56]. The velocity and pressure fields are solved implicitly in time by the generalized minimum residual. This iterative method is used to numerically solve nonsymmetric linear systems of equations by minimizing the norm of the residual vector within a Krylov subspace [57].

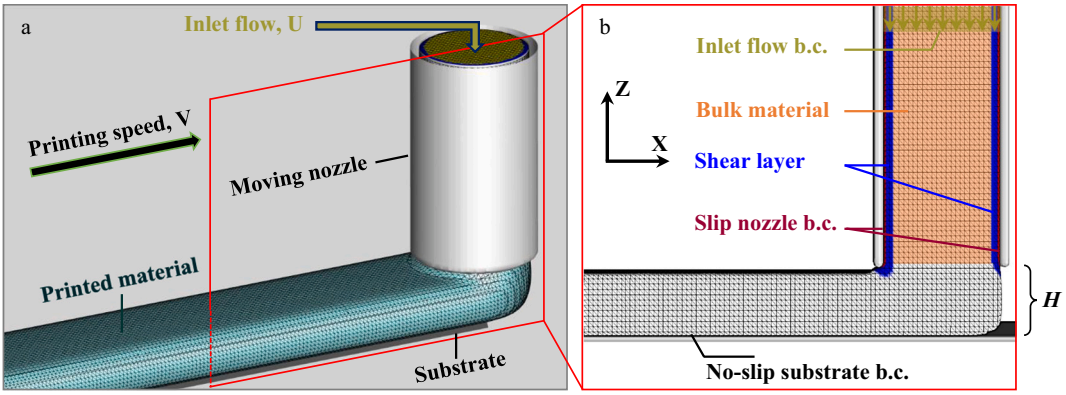

Fig. 1. Key elements of the computational domain and boundary conditions

The momentum and fluid fraction advection terms are explicitly approximated by a second-order monotonicity-preserving upwind-difference method. This discretization scheme uses a piecewise second-order polynomial approximation of the advective quantity within each cell to ensure second-order accuracy in space [58]. The time step size is determined by the solver and is controlled dynamically based on the stability and convergence criterion in order to avoid numerical instabilities [56]. The viscous stress of the momentum equation is solved implicitly using a successive under-relaxation method [59]. The Eulerian Volume of Fluid (VOF) method introduced by Hirt and Nichols [60] is adapted to flow simulations involving immiscible fluids with highly deformable interfaces. This method is used to track the free-surface flow by defining a volume fraction function α_v comprised between 0 and 1 for each grid cell classified as full, empty, or partially filled with material [61]. In these simulations, the following advection equation is used to calculate α_v:

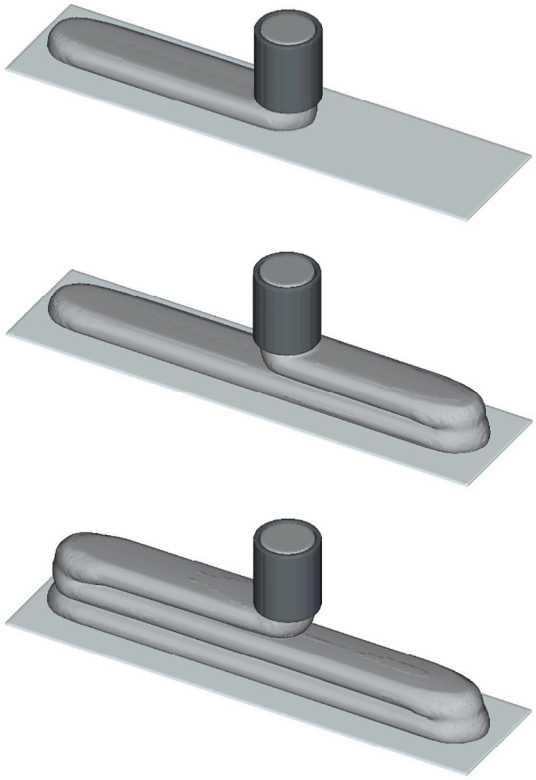

Fig. 2. Three sequences of 3D printing of the wall.

Table 2
Printing parameters of 3DCP simulations.

Case ID	Printing height H [mm]	Printing speed V [mm/s]	Extrusion speed U [mm/s]
1	7.5	50	40.5
2		40	35.1
3		30	38.2
4		20	36.3
5	12.5	50	33.4
6		40	31.6
7		30	33.6
8		20	30.8
9	17.5	50	36.9
10		40	46.1
11		30	26.7
12		20	33.6

$$\frac{\partial \alpha_v}{\partial t} + u_i \frac{\partial \alpha_v}{x_j} = 0 \tag{16}$$

The success of the VOF method strongly depends on the scheme used to discretize the convection term of the volume fraction function α_v. Therefore, special care must be taken in the discretization of this convection term in order to obtain a sharp interface. The advection equation of the VOF method is solved over time with the Split Lagrangian method known as TruVOF [55,60,61].

The numerical simulations carried out in this work consist of reproducing the 3D printing of mortar walls (Fig. 2) by a sequential extrusion of three 300 mm layers under different printing parameters (Table 2), [29].

The computational domain dimensions are set to $350 \times 80 \times 80$ mm^3 in order to form a wall by printing 300 mm long layers. As the printing path is straight, only half the domain was simulated to reduce computational time. The total number of cells of the half domain is 8 960,000 cells. The region between the nozzle orifice and the substrate is adapted to have 25 cells. The material is introduced at the nozzle inlet using a mass momentum source model [56]. The nozzle is raised of $\Delta z = H$ [mm] at the end of each deposited layer. As a result, the entire wall is obtained by continuously printing the subsequent layers without stopping the extrusion nozzle.

2.4. Mesh sensitivity analysis

A mesh sensitivity analysis was conducted using five different mesh cell sizes. The numerical simulations were performed for 300 mm long single-layer printing based on the printing parameters of case 5. The total number of cells changed from 514,550 to 9 041,382 cells (Table 3). Fig. 3 illustrates the simulated cross-sectional shapes for the five grids. It is worth noticing that the simulated cross-sectional shapes are derived by slicing a plane in the middle of each deposited layer. From the fourth grid, the simulation results were consistent and it was concluded that additional refinement was not needed. Therefore, Grid 4 involving 3 240,000 cells is adopted for all the simulations benchmark.

Table 3
Grid information for mesh sensitivity analysis.

Grid ID	Cell size [mm]	No. of cells
1	1	514,550
2	0.9	648,296
3	0.7	1,281,987
4	0.5	3,240,000
5	0.3	9,041,382

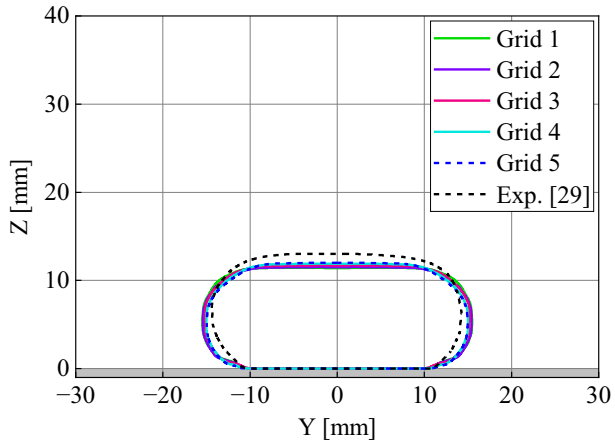

Fig. 3. Cross-sectional shape derived from mesh sensitivity analysis.

3. Results and discussion

3.1. Effect of critical shear rate on layer deposition

The critical shear rate used in the bi-viscous regularization Bingham constitutive equation [54] for the GNF modeling and is a purely numerical parameter for which the sole purpose is to avoid infinite apparent viscosity at zero shear rates. This prevents the existence of computational singularities. Therefore, choosing the optimal critical shear rate is crucial for maintaining numerical accuracy in the simulation results. Hence, a numerical analysis was conducted to investigate the sensitivity of 3D concrete printing simulations to five critical shear rate values within the range of 0.0005 s^{-1} to 0.1 s^{-1}, compared to the experimental data presented in [29]. Fig. 4 elucidates a qualitative analysis of the effect of these critical shear rates on the numerical results across six simulation cases.

The critical shear rate variation has no significant influence on the simulated cases. Indeed, the cross-sectional shapes were found almost identical, except for a minor difference observed in case 9, involving a higher speed ratio, V/U (the ratio between printing speed and extrusion speed). Furthermore, the use of smaller values of $\dot{\gamma}_c$ fails to improve the virtual outcomes when compared to the experimental data. Particularly when the geometrical ratio H/D surpasses 0.5 mm, it was noted that there is no longer contact between the substrate and the deposited layer (Fig. 5). This phenomenon is attributed to the exceptionally high apparent viscosity, resulting from the low critical shear rate values. Such high apparent viscosity leads to a very solid-like behavior of the mortar, which hinders the layer from being deposited on the substrate. Therefore, the critical shear rate value of $\dot{\gamma}_c = 0.01$ s^{-1} was found to be efficient in terms of layer shape accuracy and computational stability.

3.2. Effect of slip boundary conditions on layer deposition

Due to its granular nature, the composition of the concrete leads to slippage near the wall, the phenomenon of concrete slippage on steel has been observed and studied by Kaplan [26] who showed that when concrete flows through pipes it does not behave like a conventional fluid due to the formation of a lubricating layer at the interface between concrete/concrete and pipe wall. This layer is characterized by a slip velocity that is itself proportional to the shear stress at the wall.

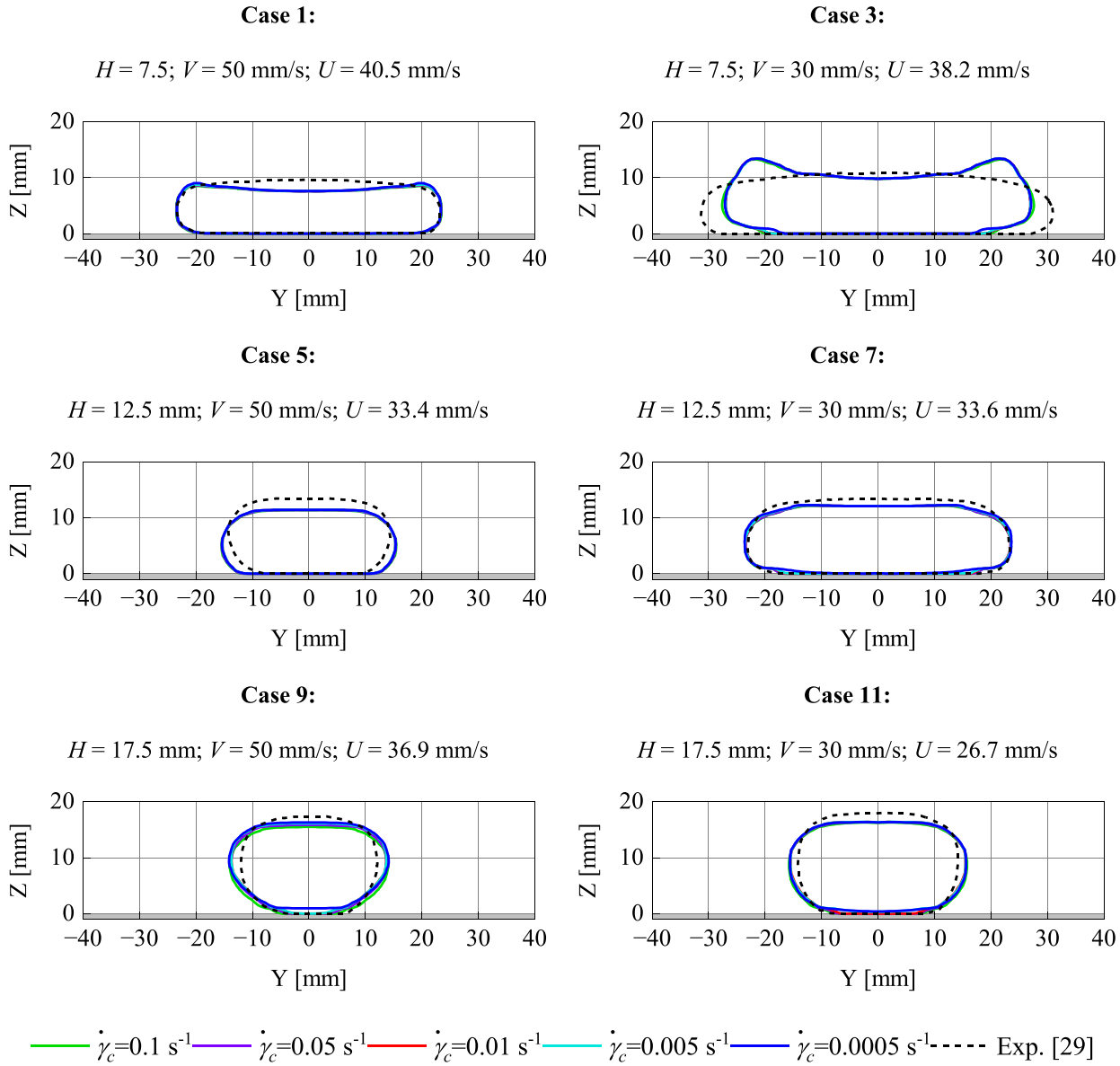

Fig. 4. Effect of fives critical shear rates on the obtained cross-sections.

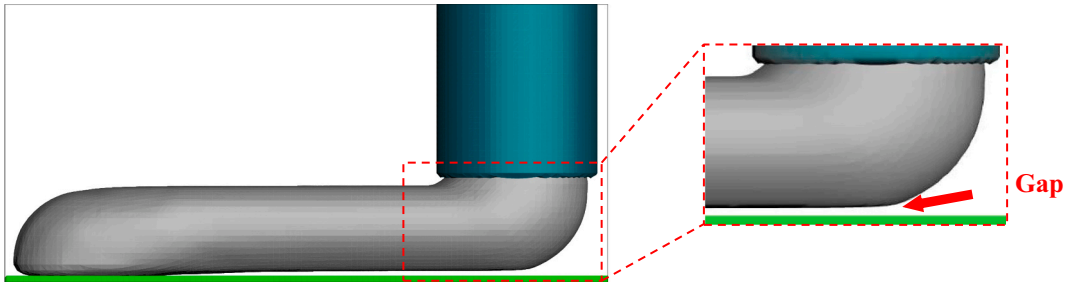

Fig. 5. Insight of gap between printed layer and substrate for case 9 (absence of contact)

Therefore, the use of free or partial slip boundary conditions turns out to be more appropriate for modeling the interaction between the concrete and nozzle wall. In this section, the influence of slip boundary conditions at the nozzle wall on the flow and stability of the simulated cross-sectional shape of the printed layers is studied. Two types of slip boundary conditions have been implemented and numerically tested: no-slip and free-slip boundary conditions (b.c.). The simulations were performed according to three printing heights H of 7.5, 12.5, and 17.5 mm, respectively. The simulated layers were printed under two different printing speeds V, mainly equal to 50 and 30 mm/s. Fig. 6 presents the cross-sectional shapes of deposited layers obtained with no-slip and free-slip boundary conditions compared to the experimental results. The simulations show that boundary conditions at the wall have a significant influence on the deposited layers.

No-slip and free-slip simulations for lower geometrical ratios and higher speed ratios (i.e., $H/D < 0.5$ and $V/U > 1$) have not shown a noticeable variation of the cross-sectional shapes compared to the experiment (case 1). On the other hand, a considerable difference in layer shape between no-slip and free-slip simulations is observed for lower geometrical- and speed-ratios (i.e., $H/D < 0.5$ and $V/U < 1$). The difference lies in an excessive deposition rate that creates swelling of the extruded material around the nozzle outlet. This might be due to the overestimation of frictional forces in the case of no-slip boundary conditions, increasing the extrusion pressure contrary to free-slip boundary conditions. Thus, strong adhesion between the extruded mortar and the substrate can create additional resistance to flow and contribute to

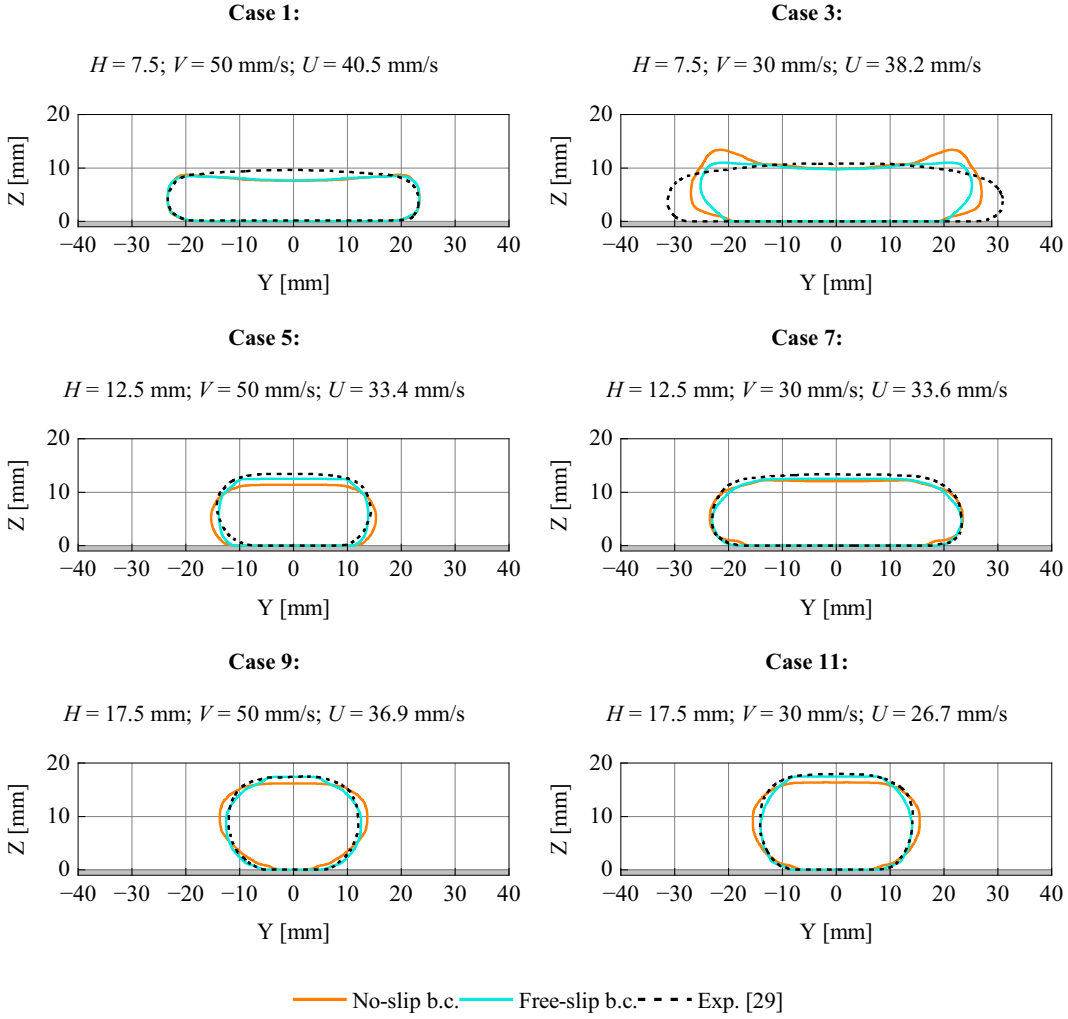

Fig. 6. Wall slip boundary conditions effect on the cross-sectional shape of the printed layers.

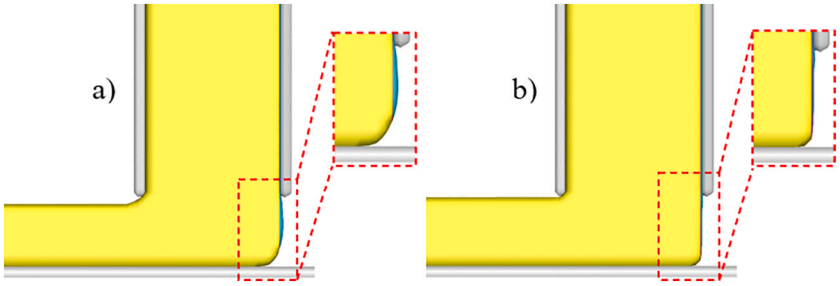

Fig. 7. Die-swell phenomenon for both a) no-slip and b) free-slip b.c.

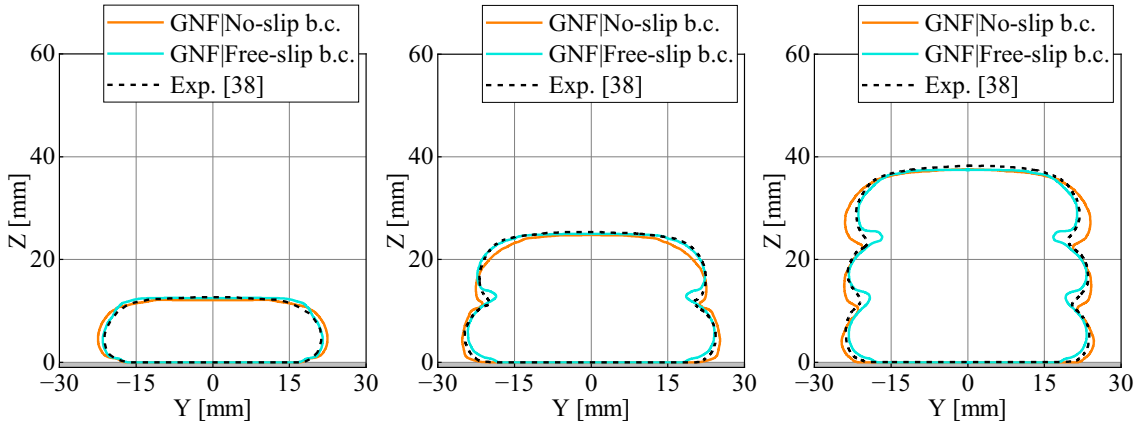

Fig. 8. Effect of slip boundary conditions on the numerical results of the GNF model (case 7).

unyielding. The predicted cross-sectional shapes were found to have better agreement with the experimental results when free-slip boundary conditions combined with higher geometrical- and speed-ratios (i.e., $H/D > 0.5$ and $V/U > 1$) were used. Fig. 7 captures a special phenomenon observed at the nozzle orifice, called "die-swell". This is a flow effect that occurs whereby the material experiences rapid stress and dimensional changes upon exiting the nozzle. Therefore, the die-swell is an important feature for the extrusion flow processing and this effect influences the final dimensions of the printed layer and imparts residual stresses. In all performed simulations, this flow characteristic is more remarkable when applying no-slip boundary conditions in contrast with free-slip boundary conditions where the die-swell does not occur.

Fig. 8 presents the cross-sectional shape of the 3D-printed wall. Particularly, the obtained results are analyzed according to the experimental 3DCP and predicted results from a CFD model provided in [38]. The numerical simulation is based on the printing parameters of case 7 while the material is modeled with the Bingham GNF model. The CFD model involving no-slip boundary conditions predicts well the experimental printing in terms of layer heights. However, a slight deformation occurring at the lateral sides is observed for the three deposited layers. Partially, this deformability could be due to the compression load distribution that strains and spreads the mortar against the substrate during simulation time. In addition, it was found that the height of the measured cross-sections slightly exceeds the height set between the nozzle and the substrate because of the hydration of the material. In contrast, the CFD model involving free-slip boundary conditions improved the predicted first printed layer. After the second and third layers have been deposited, the first layer undergoes less deformations, mainly due to the absence of shear stress between mortar and nozzle wall, thereby decreasing the extrusion pressure acting on the already deposited layer.

Moreover, a slight difference between numerical and experimental results is observed at the surface of the grooves formed by the three deposited layers. This discrepancy can be explained by the lack of modeling time-dependency of the rheological properties that were kept constant when using the Bingham GNF model along the virtual printing, while in the real experiments time dependency could be an important factor. This dependence factor stems from the thixotropy of cementitious materials, which is characterized by a rate of restructuration that evolves over the manufacturing time frame until reaches the hardened phase of the deposited layers [51]. However, in [38] a retarder admixture was used to reduce the early age of the material and its restructuration kinetics. Indeed, the printed mortar exhibits both a viscoplastic behavior when flowing and an elastic behavior at rest. The described Bingham GNF model above does not account for elastic regime which is a key characteristic in most 3DCP applications [62].

The elastic response of the material at low shear stresses could be represented through the EVP model that uses an elastic stress tensor as a source of stress in the governing equations in order to account for elastic deformation. In this case, a CFD model based on the EVP fluid and the printing parameters of case 7 was developed to reproduce the numerical simulation of the 3D-printed wall for which the cross-sectional shapes of the three stacked layers are depicted in Fig. 9. The virtual outcomes are obtained by imposing both no-slip and free-slip boundary conditions at the nozzle wall.

The results show an accurate improvement of the behavior at the layer junctions when applying free-slip boundary conditions instead of no-slip boundary conditions. Indeed, the wall shear boundary conditions involving free-slip at the nozzle wall have improved the accuracy of the numerical results for the first layer while a very small discrepancy located at the surface of the grooves coming from the layers is observed. Therefore, the EVP model was found capable of mimicking the 3DCP process more accurately. Furthermore, it is observed that the free-slip boundary conditions enhance the numerical predictions of the width

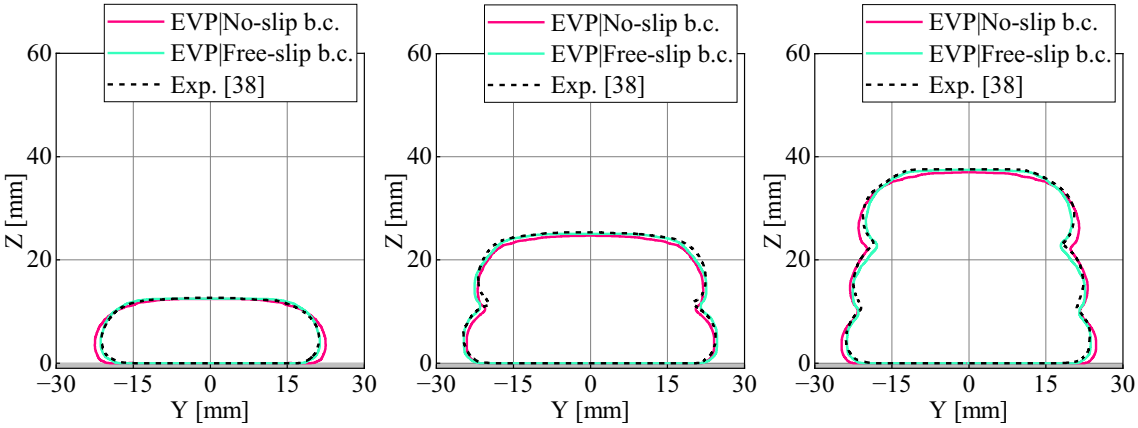

Fig. 9. Effect of slip boundary conditions on the numerical results of the EVP model (case 7).

and height of three-layers as well as the lateral sides of the wall for both rheological models.

3.3. Effect of slip boundary conditions on the extrusion pressure

The extrusion pressure reflects the compression load at the nozzle outlet required to reshape the extruded material against the substrate. This pressure is defined as the combined effect of the energy needed to spread the unyielded bulk material under interfacial friction at the nozzle wall and the plastic work expended to force and deform the yielded bulk material through the nozzle outlet. In the different printing cases, the extrusion pressure acts orthogonally and continuously onto the surface of the deposited layer as the nozzle moves along the printing path. In all simulations, the extrusion pressure was estimated by averaging the pressure values obtained at the center of cells within the nozzle outlet. The effect of slip boundary conditions on extrusion pressure is analyzed as a function of the geometrical ratio H/D and the speed ratio V/U.

No-slip conditions enforce zero velocity at the wall, causing the flowing mortar to experience shear stress due to frictional interaction with the nozzle surface. This shear stress contributes to the overall pressure buildup within the nozzle. In contrast, free-slip conditions allow the mortar to slide freely along the wall without experiencing significant shear stress. This minimizes the frictional energy dissipation and reduces the pressure required to push the material through the nozzle outlet. Therefore, the flow conditions are crucial in facilitating the flow by reducing the extrusion pressure. Table 4 summarizes the extrusion pressure reported as a function of the slip boundary conditions for different virtual printing cases.

Graphic visualization of all of these values is represented in Fig. 10. Apart from the rheological properties of the mortar, the free-slip boundary conditions were employed to tailor an understanding of the extrusion pressure dependence with respect to the applied shear stress and the printing parameters. It is observed from all simulations that the extrusion pressure decreases when employing free-slip boundary conditions despite changing the printing parameters. Furthermore, an increase in the total extrusion pressure was noticed for $V/U < 1$. This could be explained by a pressure buildup under the extrusion nozzle due to the excess amount of deposited material against the substrate, which causes ranging of the printed layer.

Table 4
Extrusion pressure for different case studies.

Case ID	Printing height H [mm]	Extrusion pressure [Pa]		Difference [Pa]
		No-slip b.c.	Free-slip b.c.	
1	7.5	7102	6365	737
2		7463	6910	553
3		8396	7700	696
4		9220	8496	725
5	12.5	1768	1162	607
6		2699	2448	251
7		4360	4119	241
8		6026	5655	372
9	17.5	1691	1220	472
10		2992	2608	384
11		2119	1601	518
12		4752	4420	333

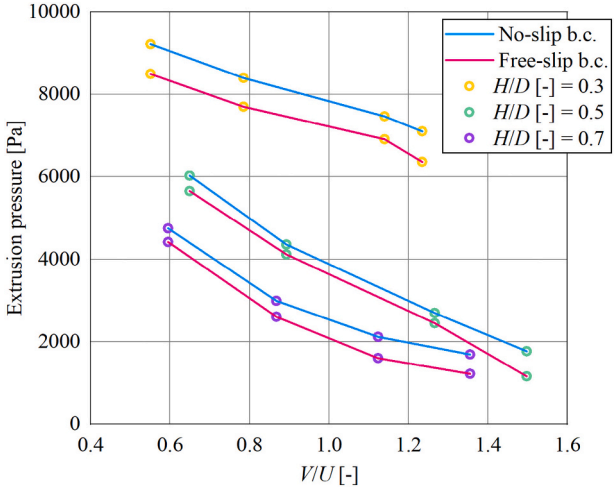

Fig. 10. Extrusion pressure of the GNF model-based simulations involving one-layer.

For lower geometrical ratios ($H/D = 0.3$), the extruded mortar consumes more extrusion pressure to spread in a limited space. Furthermore, the difference in extrusion pressure between no-slip and free-slip boundary conditions decreases as the geometrical ratio increases. This allows more space for extruding the mortar before encountering the substrate with less pronounced shear stress. However, the difference in terms of layer height decreases as the speed ratio increases (i.e., $V/U > 1$). In contrast to the no-slip boundary conditions, the layer height tends to equal the printing height when employing free-slip boundary conditions. In Fig. 11, the total extrusion pressure is analyzed as a function of slip boundary conditions while applying different geometrical- and speed-ratios for cases 1, 5, and 9.

The extrusion of mortar while the nozzle moves has created an asymmetry of the pressure distribution. This asymmetry can be attributed to the effect of flow direction, where the material encounters high resistance on the opposite side of the printing speed, leading to a pressure buildup on the left-hand side of the moving nozzle. This pressure

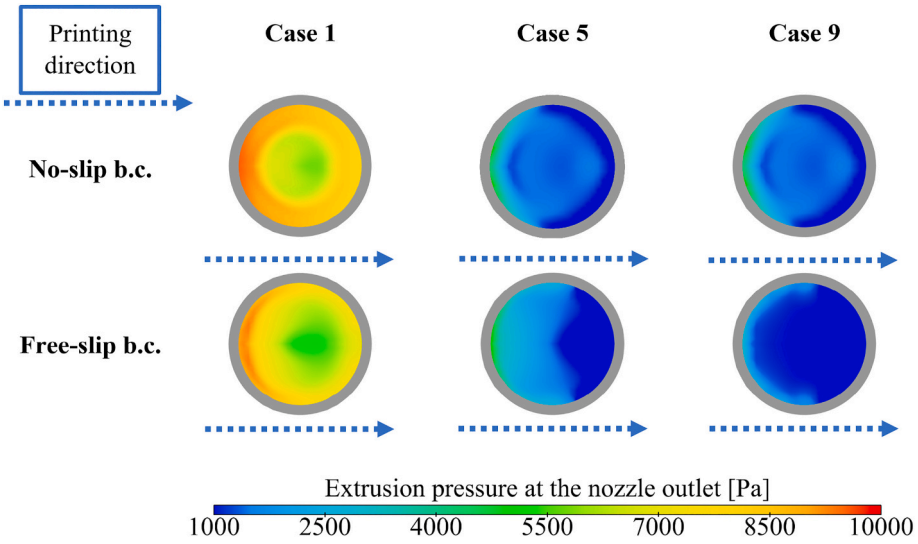

Fig. 11. Pressure distribution at nozzle orifice according to the slip boundary conditions.

imbalance results in the observed asymmetry. Fig. 12 presents the pressure distribution at the nozzle outlet for multi-layer printing of case 7 obtained with the GNF model. Multi-layer printing reveals intriguing pressure patterns. The first striking observation is the higher-pressure buildup opposite the printing direction. This stems from interfacial friction against the nozzle wall and the lack of space. Interestingly, pressure drops towards the nozzle center, reflecting the velocity profile under no-slip conditions. Free-slip simulations show a significant overall pressure decrease, highlighting the influence of interfacial friction on flow behavior. Notably, the pressure falls steadily with each subsequent layer, likely due to enlarged printing space between the nozzle outlet and substrate and potential mortar changes.

The extrusion pressure results were obtained with the GNF model. In addition, the EVP model can significantly contribute to the decrease of the estimated extrusion pressure. This is because the EVP model allows for elastic deformations under shear stresses that verify the yielding criterion $2\varepsilon/\sqrt{3} > \tau_Y/G$, where $\varepsilon = \sqrt{2tr\left(\varepsilon_{ij}^2\right)}$ is the magnitude of the small strain tensor and τ_Y/G is a material parameter that defines the plastic strain threshold. Indeed, materials that experience significant elastic deformations before yielding can demand high pressure. These materials are characterized by a high plastic strain threshold that reflects the yield stress relative to their stiffness. On the other hand, materials that deform more readily might experience less pressure buildup but may require different printing parameters. Therefore, this could be a relevant feature for optimizing the mix design and the 3D printing.

3.4. Strain rate analysis according to the slip boundary conditions

This section analyzes the effect of slip boundary conditions on the strain rate magnitude (shear rate, $\dot{\gamma}$) of the extruded material. In this regard, the CFD model provides numerical visibility into the flow behavior and enables quantification of the extent of yielded and unyielded material regions during the extrusion and deposition process, providing insights into the rate of deformation experienced by the material under different printing parameters, and even boundary conditions (no-slip versus free-slip). The strain rate distribution within the printed layers allows for identifying the intricate relation between material properties, printing parameters, and flow behavior for optimizing the 3DCP process. The distribution of the strain rate magnitude is shown for a range between 0 and 10 s^{-1} in the cross-sectional and longitudinal planes at the middle of the printed layers (cases 1, 3, 5, 7, 9, and 11) in

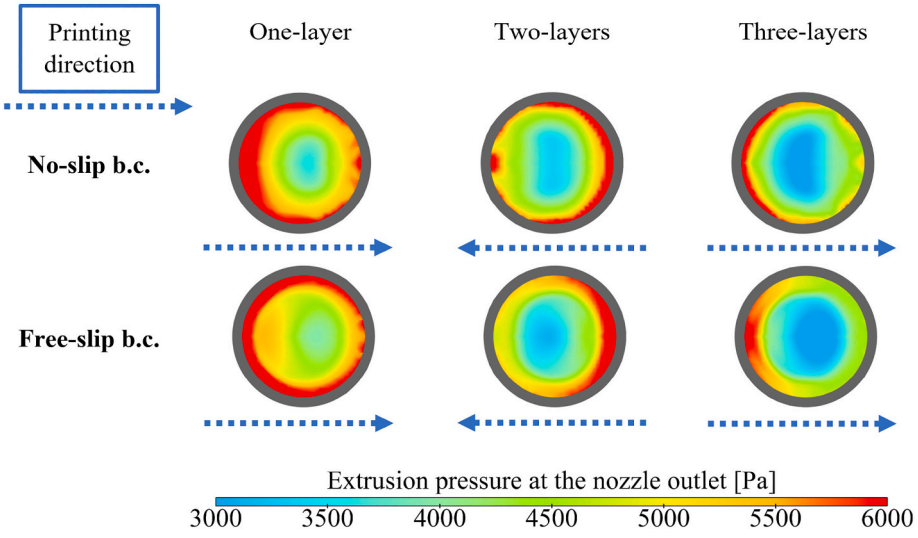

Fig. 12. Extrusion pressure at the nozzle outlet obtained with the GNF model (case 7).

Fig. 13. Analyzing variations in strain rate magnitude across both planes provides valuable insights into the spatial distribution of material properties and potential weaknesses in the printed layer.

The insights provided in Fig. 13 of strain rate distributions in mortar printing unveil a fascinating interplay between material properties, printing parameters, and boundary conditions. The presence of both yielded and unyielded regions within the printed layers stands as a testament to the Bingham GNF nature of the mortar, highlighting the critical role of overcoming the yield stress for smooth flow. The telltale shear zones near the nozzle wall, especially pronounced under no-slip conditions, speak volumes about the concentrated stress in these regions, a consequence of interfacial friction. The free-slip conditions provide a different prediction. The lower strain rates observed suggest reduced friction, leading to a more uniform pattern and a smaller unyielded core. This opens doors for exploring alternative boundary conditions to potentially achieve smoother deposition and better control over flow behavior.

Printing height also plays a key role. As we move towards higher heights (cases 5, 7, 9, and 11), the strain rates steadily decrease. This can be attributed to the gain in space, leading to lower overall shear stress. The interplay between printing and extrusion speeds further adds complexity to the equation. Higher speeds (cases 1, 5, and 9) tend to boost strain rates, expanding the yielded regions and influencing both flow dynamics and material deposition. The insights given by both cross-sectional and longitudinal planes reveal an understanding of how variations in strain rate might translate into variations in material properties

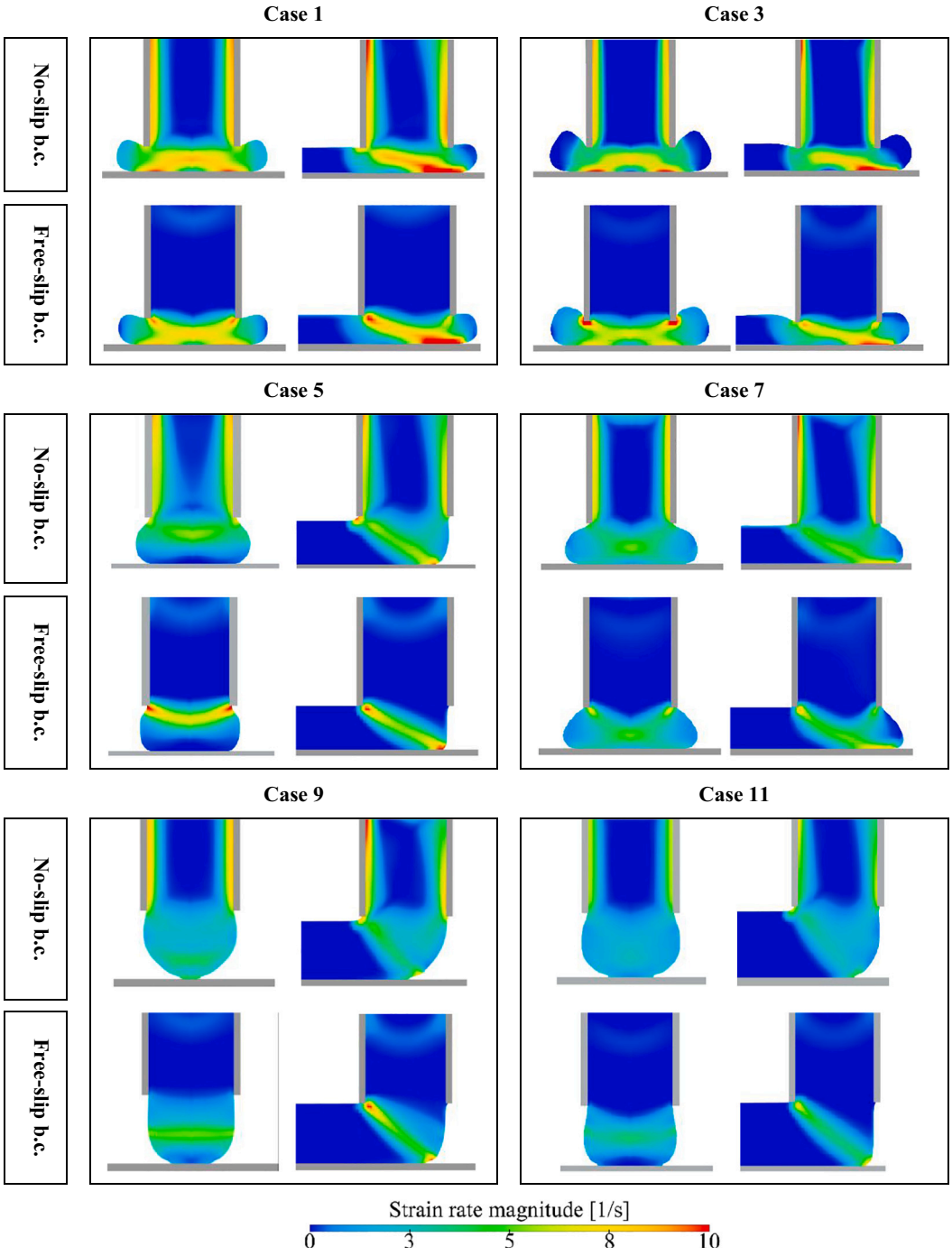

Fig. 13. Strain rate magnitude constrained by wall conditions during mortar extrusion and layer depositions.

and ultimately, the structural integrity of the printed object. Future research directions lie in validating these findings through experimentation, exploring more complex rheological models, and delving deeper into the intricacies of multi-layer printing.

4. Conclusions

This work investigated the influence of cementitious materials' slip behavior during virtual 3D printing using computational fluid dynamics. The presented models were used to replicate the experimental printing of 3D-printed walls comprising up to three layers. Specifically, the interface between the mortar and nozzle wall was modeled by free-slip boundary conditions and compared with the usual no-slip boundary conditions, mimicking more closely lubrication theory in nozzle-mortar flow. Our findings suggest that slip boundary conditions play an important role in increasing the accuracy of the predicted mortar layer shape in 3D concrete printing. The main conclusions of this work are outlined as follows:

- Simulations with the free-slip boundary conditions yield more accurate layer shapes in single and multi-layer printing compared to experiments, especially for higher geometrical ratios.
- Free-slip simulations mostly eliminate die-swell, a flow effect impacting layer shape and residual stresses, which is prominent under no-slip boundary conditions.
- Regardless of the printing parameters, free-slip boundary conditions reduce extrusion pressure compared to no-slip boundary conditions, resulting in smaller deformations of the printed layers.
- Absence of wall friction reduces the strain rate magnitude for all simulations, resulting in a more uniform velocity profile in the nozzle. However, moving beyond free-slip boundary conditions to incorporate partial slip, accounting for a proportional relationship between shear stress and slip velocity at the wall, is necessary for a more realistic simulation.

Although the inelastic GNF model with free-slip boundary conditions predicts better compared to the no-slip GNF model, it still displays a minor discrepancy at the grooves between the printed layers. This discrepancy could be due to the distribution of the yielded and the unyielded regions near the nozzle influenced by free-slip boundary conditions. The elastic EVP model with free-slip boundary conditions improves even more, the final shape of 3D-printed layers including the grooves matching the experiments almost completely. Overall, the CFD simulations provide valuable insights into the complex interplay between different boundary conditions, flow dynamics, pressure and strain rate distributions in 3D concrete printing. In the future work, the effect of free-slip boundary conditions and rheological models has to be tested for different nozzle geometries as the flow conditions may differ.

CRediT authorship contribution statement

Khalid El Abbaoui: Conceptualization, Methodology, Investigation, Formal analysis, Software, Data curation, Writing – original draft, Writing – review & editing, Visualization. **Issam Al Korachi:** Conceptualization, Methodology, Writing – original draft, Writing – review & editing, Supervision. **Mostapha El Jai:** Project administration, Supervision. **Berin Šeta:** Formal analysis, Investigation, Writing – review & editing, Visualization. **Md. Tusher Mollah:** Conceptualization, Methodology, Formal analysis, Investigation, Software, Writing – review & editing, Visualization.

Declaration of competing interest

The authors declare that they have no known competing financial interests or personal relationships that could have appeared to influence the work reported in this paper.

Acknowledgements

Not applicable.

References

[1] De Schutter G, Lesage K, Mechtcherine V, Nerella VN, Habert G, Agusti-Juan I. Vision of 3D printing with concrete—technical, economic and environmental potentials. Cem Concr Res 2018;112:25–36.
[2] Nerella VN, Näther M, Iqbal A, Butler M, Mechtcherine V. Inline quantification of extrudability of cementitious materials for digital construction. Cement and Concrete Composites. 2019;95:260–70. https://doi.org/10.1016/j.cemconcomp.2018.09.015.
[3] Ter Haar B, Kruger J, van Zijl G. Off-site construction with 3D concrete printing. Automation in Construction. 2023;152:104906. https://doi.org/10.1016/j.autcon.2023.104906.
[4] Záda V, Belda K. Structure design and solution of kinematics of robot manipulator for 3D concrete printing. IEEE Trans Autom Sci Eng 2022;19(4):3723–34. https://doi.org/10.1109/TASE.2021.3133138.
[5] Carneau P, Mesnil R, Baverel O, Roussel N. Layer pressing in concrete extrusion-based 3D-printing: experiments and analysis. Cem Concr Res 2022;155:106741. https://doi.org/10.1016/j.cemconres.2022.106741.
[6] Mechtcherine V, Bos FP, Perrot A, da Silva WL, Nerella V, Fataei S, et al. Extrusion-based additive manufacturing with cement-based materials–production steps, processes, and their underlying physics: a review. Cem Concr Res 2020;132:106037.
[7] Wan Q, Yang W, Wang L, Ma G. Global continuous path planning for 3D concrete printing multi-branched structure. Addit Manuf 2023;71:103581. https://doi.org/10.1016/j.addma.2023.103581.
[8] Bos F, Wolfs R, Ahmed Z, Salet T. Additive manufacturing of concrete in construction: potentials and challenges of 3D concrete printing. Virtual and Physical Prototyping 2016;11(3):209–25.
[9] Buswell RA, da Silva WRL, Bos FP, Schipper HR, Lowke D, Hack N, et al. A process classification framework for defining and describing digital fabrication with concrete. Cem Concr Res 2020;134:106068. https://doi.org/10.1016/j.cemconres.2020.106068.
[10] Buswell RA, De Silva WL, Jones SZ, Dirrenberger J. 3D printing using concrete extrusion: a roadmap for research. Cem Concr Res 2018;112:37–49.
[11] Boddepalli U, Panda B, Ranjani Gandhi IS. Rheology and printability of Portland cement based materials: a review. Journal of Sustainable Cement-Based Materials 2023;12(7):789–807. https://doi.org/10.1080/21650373.2022.2119620.
[12] Prevedello Rubin A, Hasse JA, Longuini Repette W. The evaluation of rheological parameters of 3D printable concretes and the effect of accelerating admixture. Construct Build Mater 2021;276:122221. https://doi.org/10.1016/j.conbuildmat.2020.122221.
[13] Roussel N. Rheological requirements for printable concretes. Cem Concr Res 2018;112:76–85.
[14] Gosselin C, Duballet R, Roux P, Gaudillière N, Dirrenberger J, Morel P. Large-scale 3D printing of ultra-high performance concrete—a new processing route for architects and builders. Mater. Des. 2016;100:102–9.
[15] Mechtcherine V, Nerella VN, Will F, Näther M, Otto J, Krause M. Large-scale digital concrete construction – CONPrint3D concept for on-site, monolithic 3D-printing. Automation in Construction 2019;107:102933. https://doi.org/10.1016/j.autcon.2019.102933.
[16] Xiao J, Ji G, Zhang Y, Ma G, Mechtcherine V, Pan J, et al. Large-scale 3D printing concrete technology: current status and future opportunities. Cement and Concrete Composites. 2021;122:104115. https://doi.org/10.1016/j.cemconcomp.2021.104115.
[17] Perrot A, Rangeard D, Nerella VN, Mechtcherine V. Extrusion of cement-based materials-an overview. RILEM Technical Letters 2018;3:91–7.
[18] Wi K, Wang K, Taylor PC, Laflamme S, Sritharan S, Qin H. Properties and microstructure of extrusion-based 3D printing mortar containing a highly flowable, rapid set grout. Cement and Concrete Composites. 2021;124:104243. https://doi.org/10.1016/j.cemconcomp.2021.104243.
[19] Nerella VN, Hempel S, Mechtcherine V. Effects of layer-interface properties on mechanical performance of concrete elements produced by extrusion-based 3D-printing. Construct Build Mater 2019;205:586–601. https://doi.org/10.1016/j.conbuildmat.2019.01.235.
[20] Ngo T, Kadri E, Bennacer R, Cussigh F. Use of tribometer to estimate interface friction and concrete boundary layer composition during the fluid concrete pumping. Construct Build Mater 2010;24(7):1253–61.
[21] Secrieru E, Khodor J, Schröfl C, Mechtcherine V. Formation of lubricating layer and flow type during pumping of cement-based materials. Construct Build Mater 2018;178:507–17. https://doi.org/10.1016/j.conbuildmat.2018.05.118.
[22] Spangenberg J, Roussel N, Hattel J, Stang H, Skocek J, Geiker M. Flow induced particle migration in fresh concrete: theoretical frame, numerical simulations and experimental results on model fluids. Cem Concr Res 2012;42(4):633–41.
[23] Xu Z, Li Z, Jiang F. Numerical approach to pipe flow of fresh concrete based on MPS method. Cem Concr Res 2022;152:106679. https://doi.org/10.1016/j.cemconres.2021.106679.
[24] Kaplan D, de Larrard F, Sedran T. Design of concrete pumping circuit. ACI Materials Journal 2005;102:110–7.

[25] Raval AD, Patel CG. Estimation of interface friction and concrete boundary layer for 3D printable concrete pumping. Materials Today: Proceedings 2022;57:664–9. https://doi.org/10.1016/j.matpr.2022.02.080.
[26] Kaplan D. Pompage des betons (concrete pumping). Etudes et recherches des laboratoires des Ponts et Chaussées, OA36; 2001.
[27] Nerella VN, Mechtcherine V. Virtual sliding pipe rheometer for estimating pumpability of concrete. Construct Build Mater 2018;170:366–77. https://doi.org/10.1016/j.conbuildmat.2018.03.003.
[28] Secrieru E, Mohamed W, Fataei S, Mechtcherine V. Assessment and prediction of concrete flow and pumping pressure in pipeline. Cement and Concrete Composites 2020;107:103495. https://doi.org/10.1016/j.cemconcomp.2019.103495.
[29] Comminal R, Leal da Silva WR, Andersen TJ, Stang H, Spangenberg J. Modelling of 3D concrete printing based on computational fluid dynamics. Cem Concr Res 2020; 138:106256. https://doi.org/10.1016/j.cemconres.2020.106256.
[30] Mohan MK, Rahul A, Van Tittelboom K, De Schutter G. Evaluating the influence of aggregate content on pumpability of 3D printable concrete. In: RILEM international conference on concrete and digital fabrication. Springer; 2020. p. 333–41.
[31] De Schryver R, El Cheikh K, Yardimci MY, Lesage K, De Schutter G. Fresh concrete pumping arrest investigation for Thixotropy by a CFD modelling approach. In: Rheology and processing of construction materials. Springer; 2019. p. 580–7.
[32] Pan T, Guo R, Fu C, Ji X, Liu Z, Yan Y. Extrusion-based 3D-concrete-printing with different flow direction. Construct Build Mater 2023;408:133714. https://doi.org/10.1016/j.conbuildmat.2023.133714.
[33] Neithalath N. Modeling of extrusion-based 3D printing of cementitious materials. American Concrete Institute; 2019.
[34] Mollah MT, Serdeczny MP, Comminal R, Seta B, Brander M, Pedersen DB, et al. A numerical investigation of the inter-layer bond and surface roughness during the yield stress buildup in wet-on-wet material extrusion additive manufacturing. In: 2022 Summer Topical Meeting: Advancing Precision in Additive Manufacturing. American Society for Precision Engineering; 2022. p. 131–4.
[35] Ooms T, Vantyghem G, Van Coile R, De Corte W. A parametric modelling strategy for the numerical simulation of 3D concrete printing with complex geometries. Addit Manuf 2021;38:101743.
[36] Reinold J, Gudžulić V, Meschke G. Computational modeling of fiber orientation during 3D-concrete-printing. Computational 2023;Mechanics:1-21.
[37] Šeta B, Sandberg M, Brander M, Mollah MT, Pokkalla D, Kumar V, et al. Modeling fiber orientation and strand shape morphology in three-dimensional material extrusion additive manufacturing. Compos Part B Eng 2023;266:110957.
[38] Spangenberg J, da Silva WRL, Comminal R, Mollah MT, Andersen TJ, Stang H. Numerical simulation of multi-layer 3D concrete printing. RILEM Technical Letters. 2021;6:119–23.
[39] Comminal R, da Silva WRL, Andersen TJ, Stang H, Spangenberg J. Influence of processing parameters on the layer geometry in 3D concrete printing: Experiments and modelling. In: RILEM international Conference on Concrete and Digital Fabrication. Springer; 2020. p. 852–62.
[40] Mollah MT, Comminal R, Serdeczny MP, Pedersen DB, Spangenberg J. Stability and deformations of deposited layers in material extrusion additive manufacturing. Addit Manuf 2021;46:102193. https://doi.org/10.1016/j.addma.2021.102193.
[41] Mollah MT, Comminal R, Serdeczny MP, Pedersen DB, Spangenberg J. Numerical predictions of bottom layer stability in material extrusion additive manufacturing. JOM 2022;74(3):1096–101.
[42] Mollah MT, Comminal R, Serdeczny MP, Šeta B, Spangenberg J. Computational analysis of yield stress buildup and stability of deposited layers in material extrusion additive manufacturing. Additive Manufacturing:103605 2023. https://doi.org/10.1016/j.addma.2023.103605.
[43] El Abbaoui K, Al Korachi I, Mollah M, Spangenberg J. Numerical modelling of planned corner deposition in 3D concrete printing. Archives of Materials Science and Engineering 2023;121(2):71–9.
[44] Mollah MT, Moetazedian A, Gleadall A, Yan J, Alphonso WE, Comminal RB, et al. Investigation on corner precision at different corner angles in material extrusion additive manufacturing: an experimental and computational fluid dynamics analysis. In: Solid Freeform Fabrication Symposium 2022: 33rd Annual Meeting. The University of Texas at Austin; 2022. p. 872–81.
[45] Mollah MT, Comminal R, Leal da Silva WR, Šeta B, Spangenberg J. Computational fluid dynamics modelling and experimental analysis of reinforcement bar integration in 3D concrete printing. Cem Concr Res 2023;173:107263. https://doi.org/10.1016/j.cemconres.2023.107263.
[46] Spangenberg J, Leal da Silva WR, Mollah MT, Comminal R, Juul Andersen T, Stang H. Integrating reinforcement with 3D concrete printing: experiments and numerical modelling. In: RILEM International Conference on Concrete and Digital Fabrication. Springer; 2022. p. 379–84.
[47] Šeta B, Mollah MT, Kumar V, Pokkalla DK, Kim S, Hassen AA, et al. Modelling fiber orientation during additive manufacturing-compression molding processes. In: 2022 International Solid Freeform Fabrication Symposium; 2022.
[48] Šeta, B., Sandberg, M., Brander, M., Mollah, M.T., Kumar Pokkalla, D., Kumar, V., Spangenberg, J.: Numerical modeling of fiber orientation in multi-layer, material-extrusion big area additive manufacturing. Material-Extrusion Big Area Additive Manufacturing.
[49] Šeta B, Sandberg M, Brander M, Mollah T, Pokkalla DK, Kumar V, et al. Numerical modeling of fiber orientation in additively manufactured composites. In: IOP Conference Series: Materials Science and Engineering. vol 1. IOP Publishing; 2023. p. 012033.
[50] Nguyen-Van V, Li S, Liu J, Nguyen K, Tran P. Modelling of 3D concrete printing process: a perspective on material and structural simulations. Addit Manuf 2023; 61:103333.
[51] Roussel N, Spangenberg J, Wallevik J, Wolfs R. Numerical simulations of concrete processing: from standard formative casting to additive manufacturing. Cem Concr Res 2020;135:106075.
[52] Perrot A, Pierre A, Nerella V, Wolfs R, Keita E, Nair S, et al. From analytical methods to numerical simulations: a process engineering toolbox for 3D concrete printing. Cement and Concrete 2021;Composites:104164.
[53] Bingham EC. An investigation of the laws of plastic flowvol. 278. US Government Printing Office; 1917.
[54] O'Donovan EJ, Tanner RI. Numerical study of the Bingham squeeze film problem. Journal of Non-Newtonian Fluid Mechanics 1984;15(1):75–83. https://doi.org/10.1016/0377-0257(84)80029-4.
[55] Hirt C, Sicilian J. A porosity technique for the definition of obstacles in rectangular cell meshes. In: International Conference on Numerical Ship Hydrodynamics, 4th; 1985.
[56] FLOW-3D®. Version 12.0 [Computer software]. Santa Fe, NM: Flow Science, Inc. https://wwwflow3dcom/; 2019.
[57] Saad Y, Schultz MH. GMRES: a generalized minimal residual algorithm for solving nonsymmetric linear systems. SIAM Journal on Scientific and Statistical Computing 1986;7(3):856–69.
[58] Van Leer B. Towards the ultimate conservative difference scheme. IV. A new approach to numerical convection. J Comput Phys 1977;23 (3):276-299. https://doi.org/10.1016/0021-9991(77)90095-X.
[59] Evans DJ, Li C. Successive underrelaxation (SUR) and generalised conjugate gradient (GCG) methods for hyperbolic difference equations on a parallel computer. Parallel Computing 1990;16(2):207–20. https://doi.org/10.1016/0167-8191(90)90059-I.
[60] Hirt CW, Nichols BD. Volume of fluid (VOF) method for the dynamics of free boundaries. J Comput Phys 1981;39(1):201–25. https://doi.org/10.1016/0021-9991(81)90145-5.
[61] Comminal R, Spangenberg J. Three-dimensional cellwise conservative unsplit geometric VOF schemes. J Comput Phys 2021;442:110479.
[62] Reiter L, Wangler T, Roussel N, Flatt RJ. The role of early age structural build-up in digital fabrication with concrete. Cem Concr Res 2018;112:86–95.